The SARS-CoV-2 conserved macrodomain is a highly efficient ADP-ribosylhydrolase enzyme

Yousef M.O. Alhammad[1], Maithri M. Kashipathy[2], Anuradha Roy[3], David K. Johnson[4], Peter McDonald[3], Kevin P. Battaile[6], Philip Gao[4], Scott Lovell[2] and Anthony R. Fehr[1,*]

[1]Department of Molecular Biosciences, University of Kansas, Lawrence, Kansas 66045, USA
[2]Protein Structure Laboratory, University of Kansas, Lawrence, Kansas 66047, USA
[3]High Throughput Screening Laboratory, University of Kansas, Lawrence, Kansas 66047, USA
[4]Molecular Graphics and Modeling Laboratory and the Computational Chemical Biology Core, University of Kansas, Lawrence, Kansas 66047, USA
[5]Protein Production Group, University of Kansas, Lawrence, Kansas 66047, USA
[6]NYX, New York Structural Biology Center, Upton, NY 11973, USA

*****Correspondence: arfehr@ku.edu; Tel.: +1- (785) 864-6626 (K.S.)

Running title: SARS-CoV-2 Mac1 removes ADP-ribose from protein *in vitro*

Keywords: Coronavirus, SARS-CoV-2, macrodomain, ADP-ribose

ABSTRACT

Severe acute respiratory syndrome coronavirus 2 (SARS-CoV-2) and other SARS-like-CoVs encode 3 tandem macrodomains within non-structural protein 3 (nsp3). The first of these macrodomains, termed Mac1, is conserved throughout CoVs, binds to mono- and poly-ADP-ribose, and hydrolyzes mono-ADP-ribose (MAR) from target proteins. Mac1 is essential for pathogenesis in multiple animal models of CoV infection, implicating this domain as a prominent virulence factor and potential therapeutic target. Mac1 likely counters host-mediated antiviral ADP-ribosylation, a posttranslational modification that is part of the host response to viral infections. Here we report the crystal structure of SARS-CoV-2 Mac1 in complex with ADP-ribose refined at 2.2 Å resolution. SARS-CoV-2, SARS-CoV and MERS-CoV Mac1 exhibit similar structural folds and ADP-ribose binding modes as shown by structural comparison. All three CoV Mac1 proteins bound to ADP-ribose with low μM affinities. They also demonstrated highly efficient de-MARylating activity, which was greater than that of the human Mdo2 macrodomain. We conclude that the SARS-CoV-2 and other CoV Mac1 proteins are highly efficient ADP-ribosylhydrolases with strikingly similar activity, indicating that compounds targeting CoV Mac1 proteins may have broad antiviral activity against CoVs.

IMPORTANCE

SARS-CoV-2 has recently emerged into the human population and has led to a worldwide pandemic of COVID-19 that has caused nearly 300K deaths worldwide. With, no currently approved treatments, novel therapeutic strategies are desperately needed. All coronaviruses encode for a highly conserved macrodomain (Mac1) that binds to and removes ADP-ribose, a post-translation modification, from proteins. This protein domain is essential for CoV pathogenesis and may be a novel therapeutic target. Thus, understanding its biochemistry and enzyme activity are critical first steps for these efforts. Here we report the crystal structure of SARS-CoV-2 Mac1 in complex with ADP-ribose, and describe its ADP-ribose binding and hydrolysis activities in direct comparison to SARS-CoV and MERS-CoV Mac1 proteins, and a human macrodomain. These results are an important first step for the design and testing of potential therapies targeting this unique protein domain.

INTRODUCTION

The recently emerged pandemic outbreak of COVID-19 is caused by a novel coronavirus named severe acute respiratory syndrome coronavirus 2 (SARS-CoV-2)[1,2]. As of May 11, 2020 this virus is responsible for ~ 4 million cases of COVID-19 and >285,000 deaths worldwide. SARS-CoV-2 is a member of the lineage B β-CoVs with overall high sequence similarity with other SARS-like CoVs, including SARS-CoV. While most of the genome is >80% similar with SARS-CoV, there are regions where amino acid conservation is significantly lower. As expected, the most divergent proteins in the SARS-CoV-2 genome from SARS-CoV include the Spike glycoprotein and several accessory proteins including 8a (absent), 8b (extended), and 3b (truncated). However, somewhat unexpectedly, several non-structural proteins also show significant divergence from SARS-CoV, including non-structural proteins 3, 4, and 7, which could affect the biology of SARS-CoV-2[3,4].

Coronaviruses encode 16 non-structural proteins that are translated from two open reading frames (ORFs), replicase 1a and 1ab (rep1a and rep1ab)[5]. The largest non-structural protein is non-structural protein 3 (nsp3) that encodes for multiple modular protein domains. These domains in SARS-CoV-2 diverge in amino acid sequence from SARS-CoV as much as 30%, and it includes a large insertion of 25-41 residues just upstream of the first of three tandem macrodomains (Mac1, Mac2, and Mac3) (Fig. 1A)[3]. In addition to this insertion, the individual macrodomains show large amounts of amino acid divergence. Mac1 diverges 28% from SARS-CoV and 59% from MERS-CoV, while Mac2 and Mac3 diverge 24% from SARS-CoV. It is feasible that these significant sequence differences could impact the unique biology of SARS-CoV-2. However, macrodomains have a highly conserved structure, and thus sequence divergence may have little impact on their overall function. Mac1 is present in all CoVs, unlike

Mac2 and Mac3, and early structural and biochemical data demonstrated that it contains a conserved three-layered α/β/α fold and binds to ADP-ribose, poly-ADP-ribose, and other related molecules[6-10]. ADP-ribose is buried in a hydrophobic cleft where the ADP-ribose binds to several highly-conserved residues such as aspartic acid at position 23 (D23) and asparagine at position 41 (N41) of SARS-CoV[6]. Mac1 homologs are also found in alphaviruses, Hepatitis E virus, and Rubella virus, and structural analysis of these macrodomains have demonstrated that they are very similar to CoV Mac1[11,12] and are all members of the larger MacroD-type macrodomain family, which includes human macrodomains Mdo1 and Mdo2[13].

The CoV Mac1 was originally called an ADP-ribose-1”-phosphatase (ADRP) based on data demonstrating that it could remove the phosphate group from ADP-ribose-1”-phosphate[6-8]. However, the activity was rather modest, and it was unclear why this would impact a virus infection. More recently it has been demonstrated that CoV Mac1 can hydrolyze the bond between amino acid chains and ADP-ribose molecules[14-16], indicating that it can reverse protein ADP-ribosylation[6,8]. ADP-ribosylation is a post-translational modification catalyzed by ADP-ribosyltransferases (also known as PARPs) through transferring an ADP-ribose moiety from NAD^+ onto target proteins[17]. The ADP-ribose is transferred as single mono-ADP-ribose unit (MAR), or single units of ADP-ribose are transferred consecutively to form a poly-ADP-ribose chain (PAR). CoV Mac1 efficiently hydrolyzes MAR, but has minimal activity against PAR[14,15]. Several MARylating PARPs are induced by interferon (IFN) and are known to inhibit virus replication, implicating ADP-ribosylation in the host-response to infection[18].

Several reports have addressed the role of Mac1 on the replication and pathogenesis of CoVs, mostly using the mutation of a highly conserved asparagine to alanine. This mutation abolished the ADP-ribosylhydrolase activity of SARS-CoV Mac1[16]. This mutation has minimal

effects on virus replication in transformed cells, but reduces viral load, leads to enhanced IFN production, and strongly attenuates both Murine Hepatitis Virus (MHV) and SARS-CoV in mouse models of infection[7,16,19,20]. MHV Mac1 was also required for efficient replication in primary macrophages, which could be partially rescued by PARP inhibitors or siRNA knockdown of PARP12 or PARP14[21]. These data suggest that Mac1's likely function is to counter PARP-mediated anti-viral ADP-ribosylation[22]. Mutations in the alphavirus and HEV macrodomain are also known to have substantial phenotypic effects on virus replication and pathogenesis[14,23-26]. As viral macrodomains are clearly important virulence factors, they are considered to be potential targets for anti-viral therapeutics[22].

Based on the close structural and functional similarities between viral macrodomains we hypothesized that SARS-CoV-2 Mac1 has similar binding and hydrolysis activity as other CoV Mac1 enzymes. In this study, we determined the crystal structure of the SARS-CoV-2 Mac1 protein bound to ADP-ribose. Binding to ADP-ribose was further confirmed and directly compared to a human macrodomain (Mdo2) and the SARS-CoV and MERS-CoV Mac1 proteins by several *in vitro* assays. Finally, using an auto-modified protein substrate, we demonstrated that SARS-CoV-2, SARS-CoV, and MERS-CoV Mac1 proteins are very efficient ADP-ribosylhydrolases. These results will be instrumental in the design and testing of novel therapeutic agents targeting the CoV Mac1 protein domain.

RESULTS

Structure of the SARS-CoV-2 Mac1 complexed with ADP-ribose. To create recombinant SARS-CoV-2 Mac1 for structure determination and enzyme assays, nucleotides 3348-3872 of SARS-CoV-2 isolate Wuhan-hu-1, representing amino acids I1023-K1197 of rep1a, were cloned into a bacterial expression vector containing an N-terminal His tag and TEV cleavage site. We obtained large amounts (>100 mg) of highly purified recombinant protein (Fig. S1A). A small amount of this protein was digested by the TEV protease to obtain protein devoid of any extra tags for crystallization and used to obtain crystals from which the structure was determined (Fig. S1B). Our crystallization experiments resulted in the same crystal form (needle clusters) from several conditions, but only when ADP-ribose was added to the protein. This represents an additional crystal form ($P2_1$) amongst the recently determined SARS-CoV-2 macrodomain structures[27-29].

The structure of SARS-CoV-2 Mac1 complexed with ADP-ribose was obtained using X-ray diffraction data to 2.2 Å resolution and contained four molecules in the asymmetric unit that were nearly identical. The polypeptide chains could be traced from V3-M171 for subunits A/C and V3-K172 for subunits B/D. Superposition of subunits B-D onto subunit A (169 residues aligned) yielded RMSD deviations of 0.17 Å, 0.17 Å and 0.18 Å respectively between Cα atoms. As such, subunit A was used for the majority of the structure analysis described herein. The SARS-CoV-2 Mac1 protein adopted a fold consistent with the MacroD subfamily of macrodomains that contains a core composed of a mixed arrangement of 7 β-sheets (parallel and antiparallel) that are flanked by 6 α-helices (Fig. 2A-B).

As mentioned above, apo crystals were never observed for our construct, though the apo structure has been solved by researchers at The Center for Structural Genomics of Infectious

Diseases (PDB 6WEN)[28] and University of Wisconsin-Milwaukee (PDB 6WEY)[27]. Further analysis of the amino acid sequences used for expression and purification revealed that our construct had 5 additional residues at the C-terminus (MKSEK) and differs slightly at the N-terminus as well (GIE vs GE) relative to 6WEN. In addition, the sequence used to obtain the structure of 6WEY is slightly shorter than SARS-CoV-2 Mac1 at both the N and C-terminal regions (Fig. S2A). To assess the effect of these additional residues on crystallization, chain B of the SARS-CoV-2 Mac1, which was traced to residue K172, was superimposed onto subunit A of PDB 6W02[29], a previously determined structure of ADP-ribose bound SARS-CoV-2 Mac1. Analysis of the crystal packing of 6W02 indicates that the additional residues at the C-terminus would clash with symmetry related molecules (Fig. S2B). This suggests that the presence of these extra residues at the C-terminus likely prevented the generation of the more tightly packed crystal forms obtained for 6W02 and 6WEY, which diffracted to high resolution.

The ADP-ribose binding pocket contained large regions of positive electron density consistent with ADP-ribose molecules (Fig. 3A). The adenine forms two hydrogen bonds with D22-I23, which makes up a small loop between β2 and the N-terminal half of α1. The side chain of D22 interacts with N6, while the backbone nitrogen atom of I23 interacts with N1, in a very similar fashion to the SARS-CoV macrodomain[6]. A large number of contacts are made in the loop between β3 and α2 which includes many highly-conserved residues, including a GGG (motif) and N40, which is completely conserved in all enzymatically active macrodomains[30]. N40 is positioned to make hydrogen bonds with the 3' OH groups of the distal ribose, as well as a conserved water molecule. K44 and G46 also make hydrogen bonds with the 2' OH of the distal ribose, G48 makes contact with the 1' OH and a water that resides near the catalytic site, while the backbone nitrogen atom of V49 hydrogen bonds with the α-phosphate. The other major

interactions with ADP-ribose occur in residues G130, I131, and F132 that are in the loop between β6 and α5 (Fig. 3B). The α-phosphate accepts a hydrogen bond from the nitrogen atom of I131, while the β-phosphate accepts hydrogen bonds from the backbone nitrogen atom of G130 and F132. Loops β3-α2 and β6-α5 are connected by an isoleucine bridge that forms a narrow channel around the diphosphate which helps position the terminal ribose for water-mediated catalysis[6]. Additionally, a network of direct contacts of ADP-ribose to solvent along with water mediated contacts to the protein are shown (Fig. 3C).

Comparison of SARS-CoV-2 with other CoV macrodomain structures. We next sought to compare the SARS-CoV-2 Mac1 to other deposited structures of this protein. Superposition with Apo (6WEN) and ADP-ribose complexed protein (6W02) yielded RMSD of 0.48 Å (168 residues) and 0.37 Å (165 residues), respectively, indicating a high degree of similarity (Fig. S3A-B). Comparison of the ADP-ribose binding site of SARS-CoV-2 Mac1 with that of the apo structure (6WEN) revealed minor conformational differences in order to accommodate ADP-ribose binding. The loop between β3 and α2 (H45-V49) undergoes a change in conformation and the sidechain of F132 is moved out of the ADP-ribose binding site (Fig. S3C). Our ADP-ribose bound structure is nearly identical to 6W02, except for slight deviations in the β3-α2 loop and an altered conformation of F156, where the aryl ring of F156 is moved closer to the adenine ring (Fig. S3 C-D). However, this is likely a result of crystal packing as F156 adopts this conformation in each subunit and would likely clash with subunit residues related by either crystallographic or non-crystallographic symmetry.

We next compared the ADP-ribose bound SARS-CoV-2 Mac1 structure with that of SARS-CoV (PDB 2FAV) and MERS-CoV (PDB 5HOL) Mac1 proteins. Superposition yielded RMSD deviations of 0.71 Å (166 residues) and 1.06 Å (161 residues) for 2FAV and 5HOL,

183 respectively. Additionally, the ADP-ribose binding mode in the SARS-CoV and SARS-CoV-2
184 structures almost perfectly superimposed (Fig. 4 A-D). The conserved aspartic acid residue
185 (D22, SARS-CoV-2) that binds to adenine, are localized in a similar region although there are
186 slight differences in the rotamers about the Cβ-Cγ bond. The angles between the mean planes
187 defined by the OD1, CG and OD2 atoms relative to SARS-CoV-2 Mac1 is 23.1^{o} and 46.5^{o} for
188 the SARS-CoV and MERS-CoV Mac1 structures, respectively. Another notable difference is
189 that SARS-CoV and SARS-CoV-2 macrodomains have an isoleucine (I23) following this
190 aspartic acid while MERS-CoV has an alanine (A22). Conversely, SARS-CoV-2 and SARS-
191 CoV Mac1 have a valine instead of an isoleucine immediately following the GGG motif
192 (V49/I48). From these structures it appears that having two isoleucines in this location would
193 clash, and that lineage B and lineage C β-CoVs has evolved in unique ways to create space in
194 this pocket (Fig. 4D and data not shown). Despite these small differences in local structure, the
195 overall structure of CoV Mac1 domains remain remarkably conserved, and indicates they likely
196 have similar biochemical activities and biological functions.

197 **SARS-CoV, SARS-CoV-2, and MERS-CoV bind to ADP-ribose with similar**
198 **affinities.** To determine if the CoV macrodomains had any noticeable differences in their ability
199 to bind ADP-ribose, we performed isothermal titration calorimetry (ITC), which measures the
200 energy released or absorbed during a binding reaction. Macrodomain proteins from human
201 (Mdo2), SARS-CoV, MERS-CoV, and SARS-CoV-2 were purified (Fig. S1A) and tested for
202 their affinity to ADP-ribose. All CoV Mac1 proteins bound to ADP-ribose with low micromolar
203 affinity (7-16 μM), while human Mdo2 bound with an affinity about 10-times stronger (~220
204 nM) (Fig. 5A-B). As a control we tested the ability of the MERS-CoV macrodomain to bind to
205 ATP, and only observed minimal binding with mM affinity (data not shown). At higher

206 concentrations, the SARS-CoV-2 macrodomain caused a slightly endothermic reaction,
207 potentially the result of protein aggregation or a change in conformation (Fig. 5A). The MERS-
208 CoV Mac1 had a greater affinity for ADP-ribose than SARS-CoV or SARS-CoV-2 Mac1 in the
209 ITC assay (Fig. 5A-B), however, our results found the differences between these macrodomain
210 proteins to be much closer than previously reported[9]. As an alternate method to confirm ADP-
211 ribose binding, we conducted a thermal shift assay. All 4 macrodomains tested denatured at
212 higher temperatures with the addition of ADP-ribose (Fig. 5C). We conclude that lineage B and
213 lineage C β-CoV Mac1 proteins bind to ADP-ribose with similar affinities.

214 **CoV macrodomains are highly efficient mono-ADP-ribosylhydrolases.** To examine
215 the ADP-ribosylhydrolase activity of coronaviruses Mac1, we first tested the viability of using
216 antibodies to detect mono-ADP-ribosylated protein. Previously, only radiolabeled NAD^+ has
217 been used to label ADP-ribosylated protein[14,15]. To create a mono-ADP-ribosylated substrate, the
218 catalytic domain of the PARP10 (GST-PARP10 CD) protein was incubated with NAD^+, leading
219 to its auto-ADP-ribosylation. We then tested a panel of monoclonal antibodies that detect mono-
220 ADP-ribose (MAR), poly-ADP-ribose (PAR), or both MAR and PAR for the ability to detect
221 MARylated PARP10. The anti-MAR and anti-MAR/PAR antibodies, but not anti-PAR antibody,
222 bound to MARylated PARP10 (Fig. S4). From herein we utilized the anti-MAR antibody to
223 detect ADP-ribosylated PARP10.

224 We next tested the ability of SARS-CoV-2 Mac1 to remove ADP-ribose from
225 MARylated PARP10. SARS-CoV-2 Mac1 and MARylated PARP10 were incubated at
226 equimolar amounts of protein at 37 ^oC and the reaction was stopped at 5, 10, 20, 30, 45 or 60
227 minutes (Fig. 6A). As a control, MARylated PARP10 was incubated alone for 60 minutes at
228 37^oC. Each reaction had equivalent amounts of MARylated PARP10 and Mac1 which was

confirmed by Coomassie Blue staining (Fig. 6A). An immediate reduction of more than 50% band intensity was observed within five minutes, and the ADP-ribose modification was nearly completely removed by SARS-CoV-2 Mac1 within 30 minutes (Fig. 6A). The MARylated PAPR10 bands intensities were calculated, plotted, and fit to a non-linear regression curve (Fig. 6B). This result indicates that the SARS-CoV-2 Mac1 protein is a highly efficient ADP-ribosylhydrolase.

Next, we compared ADP-ribosylhydrolase activity of Mac1 from SARS-CoV-2, SARS-CoV, and MERS-CoV and human Mdo2. These proteins were incubated with MARylated PARP10 as described above and the removal of MAR was analyzed at 5, 15 and 30 minutes (Fig. 6C). MAR was rapidly removed from MARylated PARP10 with the CoV Mac1 proteins (Fig. 6D). Approximately 95% of MAR was removed by SARS-CoV and SARS-CoV-2 Mac1 within 15 minutes, while at the same timepoint MERS-CoV Mac1 removed about 85% of MAR (Fig. 6D). A more gradual decrease of MARylated PAPR10 band intensity was observed with Mdo2. It removed approximately 70% of MAR in 30 minutes, which was significantly different from both SARS-CoV and SARS-CoV-2 Mac1. These data showed that CoV Mac1 proteins have similar ADP-ribosylhydrolase activity against an auto-modified PARP10 protein and have increased activity when compared to the human Mdo2 protein for this substrate under these conditions. However, further enzymatic analyses of these proteins are warranted to more thoroughly understand their kinetics and affinities for ADP-ribosylated substrates.

DISCUSSION

Here we report the crystal structure of SARS-CoV-2 Mac1. It has a conserved three-layered α/β/α fold typical of the MacroD family of macrodomains, and is extremely similar to other CoV Mac1 proteins (Fig. 2-4). The conserved coronavirus macrodomain (Mac1) was initially described as an ADP-ribose-1"-phosphatase (ADRP), as it was shown to be structurally similar to yeast enzymes that have this enzymatic activity[31]. Early biochemical studies confirmed this activity for CoV Mac1, though its phosphatase activity for this substrate was rather modest[6-8]. Later, it was shown that mammalian macrodomain proteins could remove ADP-ribose from protein substrates, indicating protein de-ADP-ribosylation as a more likely function for the viral macrodomains[30,32,33]. Shortly thereafter, the SARS-CoV, hCoV-229E, FIPV, several alphavirus, and the hepatitis E virus macrodomains were demonstrated to have de-ADP-ribosylating activity [14-16]. However, this activity has not yet been reported for the MERS-CoV or SARS-CoV-2 Mac1 protein. In this study, we show that the Mac1 proteins from SARS-CoV, MERS-CoV and SARS-CoV-2 hydrolyze ADP-ribose from a protein substrate (Fig. 6). Their activities were similar despite sequence divergence of almost 60% between SARS-CoV-2 and MERS-CoV. We then compared these activities to the human Mdo2 macrodomain. Mdo2 had a greater affinity for ADP-ribose than the viral enzymes, but had significantly reduced enzyme activity in our experiments. These results suggest that the human and viral enzymes have sufficient structural differences that result in differences in biochemical activities. Finally, while all previous studies of macrodomain de-ADP-ribosylation had used radiolabeled substrate, we obtained highly repeatable and robust data utilizing antibodies designed to specifically recognized mono-ADP-ribose[34]. The use of these antibodies should enhance the feasibility of this assay for many labs that are not equipped for radioactive work.

The functional importance of Mac1 has been demonstrated in several reports, mostly utilizing the mutation of a highly conserved asparagine that mediates contact with the distal ribose (Fig. 3B)[16,19,20]. From these reports it is clear that CoV Mac1 is vital for the ability of these viruses to cause disease, and have indicated that it could be a novel therapeutic target. Despite this, there are no known compounds that inhibit this domain. The outbreak of COVID-19 has illustrated an incredible need for developing multiple therapeutic drugs targeting conserved coronavirus proteins. Mac1 appears to be an ideal candidate for further drug development based on its: *i)* highly conserved structure and biochemical activities within CoVs; and *ii)* its clear importance for multiple CoVs to cause disease. Targeting Mac1 may also have the benefit of enhancing the innate immune response, as we have shown that Mac1 is required for some CoVs to block IFN production[16,21]. Considering that Mac1 from divergent αCoVs such as 229E and FIPV also have de-ADP-ribosylating activity[14,15], it is also possible that compounds targeting Mac1 could prevent disease caused by of wide variety of CoV, including those of veterinary importance like porcine epidemic diarrhea virus (PEDV). Further, compounds that inhibit Mac1 could help identify its protein targets during infection. Future studies could utilize the SARS-CoV-2 Mac1 structure to identify the mechanisms it uses to bind to its biologically relevant protein substrates, remove ADP-ribose from these proteins, and potentially define the precise function for Mac1 in CoV replication and pathogenesis. These studies will be critical for the design and development of highly-specific Mac1 inhibitors that could be used therapeutically to mitigate COVID-19 or future CoV outbreaks.

METHODS

Plasmids

The SARS-CoV macrodomain (Mac1) (residues 1000-1172 of pp1a) was cloned into the pET21a+ expression vector with an N-terminal His tag. The MERS-CoV Mac1 (residues 1110-1273 of pp1a) was also cloned into pET21a+ with a C-terminal His tag. SARS-CoV-2 Mac1 (residues 1023-1197 of pp1a) was cloned into the pET30a+ expression vector with an N-terminal His tag and a TEV cleavage site (Synbio). The pETM-CN Mdo2 Mac1 (residues 7-243) expression vector with an N-terminal His-TEV-V5 tag and the pGEX4T-PARP10CD (residues 818-1025) expression vector with an N-terminal GST tag were previously described[30] (Ivan Ahel, Oxford University). All plasmids were confirmed by restriction digest, PCR, and direct sequencing.

Protein Expression and Purification

A single colony of *E. coli* cells (C41(DE3)) containing plasmids harboring the constructs of the macrodomain proteins was inoculated into 10mL LB media and grown overnight at 37°C with shaking at 250 rpm. The overnight culture was transferred to a shaker flask containing 2X 1L TB media at 37^{o}C until the OD600 reached to about 0.7. The proteins were either induced with 0.4 mM IPTG at 37C for 3 hours, or 17°C for 20 hours. Cells were pelleted at 3500 × g for 10 min and frozen at -80°C. Frozen cells were thawed at room temperature, resuspended in 50mM tris (pH 7.6), 150mM NaCl, and sonicated using the following cycle parameters: Amplitude: 50%, Pulse length: 30 seconds, Number of pulses: 12, while incubating on ice for >1min between pulses. The soluble fraction was obtained by centrifuging the cell lysate at 45,450 × g for 30 minutes at 4°C. The expressed soluble proteins were purified by affinity chromatography using a 5 ml prepacked HisTrap HP column on an AKTA Pure protein

purification system (GE Healthcare). The fractions were further purified by size-exclusion chromatography (SEC) with a Superdex 75 10/300 GL column equilibrated with 20mM Tris (pH 8.0), 150 mM NaCl and the protein sized as a monomer relative to the column calibration standards. To cleave off the His tag from the SARS-CoV-2 Mac1, purified TEV protease was added to purified SARS-CoV-2 Mac1 protein at a ratio of 1:10 (w/w), and then passed back through the Ni-NTA HP column. Protein was collected in the flow through and equilibrated with 20mM Tris (pH 8.0), 150 mM NaCl. The SARS-CoV-2 Mac1, free from the N-terminal His tag, was used for subsequent crystallization experiments.

For the PARP 10 protein, the cell pellet was resuspended in in 50mM Tris-HCl (pH 8.0), 500mM NaCl, 0.1mM EDTA, 25% glycerol, 1mM DTT and sonicated as described above. The cell lysate was incubated with 10 ml of Glutathione Sepharose 4B resin from GE Healthcare, equilibrated with the same buffer for 2 hours, then applied to a gravity flow column to allow unbound proteins to flow through. The column was washed with the resuspension buffer till the absorbance at 280 nm reached baseline. The bound protein was eluted out of the column with resuspension buffer containing 20mM reduced glutathione and then dialyzed back into the resuspension buffer overnight at 4°C.

Isothermal Titration Calorimetry

All ITC titrations were performed on a MicroCal PEAQ-ITC instrument (Malvern Pananalytical Inc., MA). All reactions were performed in 20 mM Tris pH 7.5, 150 mM NaCl using 100 uM of all macrodomain proteins at 25°C. Titration of 2 mM ADP-ribose or ATP (MilliporeSigma) contained in the stirring syringe included a single 0.4 µL injection, followed by 18 consecutive injections of 2 µL. Data analysis of thermograms was analyzed using one set of

binding sites model of the MicroCal ITC software to obtain all fitting model parameters for the experiments.

Differential Scanning Fluorimetry (DSF)

Thermal shift assay with DSF involved use of LightCycler® 480 Instrument (Roche Diagnostics). In total, a 15µl mixture containing 8X SYPRO Orange (Invitrogen), and 10 uM Mac1 protein in buffer containing 20 mM Hepes, NaOH, pH 7.5 and various concentrations of ADP-ribose were mixed on ice in 384-well PCR plate (Roche). Fluorescent signals were measured from 25 to 95 °C in 0.2 °C/30-s steps (excitation, 470–505 nm; detection, 540–700 nm). The main measurements were carried out in triplicate. Data evaluation and Tm determination involved use of the Roche LightCycler® 480 Protein Melting Analysis software, and data fitting calculations involved the use of single site binding curve analysis on Graphpad Prism.

DeMARylation Assay

Automodification of PARP10 protein: A 10 µM solution of purified PAPR10 protein was incubated for 20 minutes at 37^{o}C with 1mM final concentration of β-Nicotinamide adenine dinucleotide (β NAD+) (Millipore-Sigma) in a reaction buffer (50mM HEPES, 150mM NaCl, 0.2MM DTT, and 0.02% NP-40). MARylated PARP10 was aliquoted and stored at -80^{o}C.

PAPR10 ADP-ribose hydrolysis: All reactions were performed at 37^{o}C for the designated time. One µmol of MARylated PARP10 and purified Mac1 protein was added in the reaction buffer (50mM HEPES, 150mM NaCl, 0.2MM DTT, and 0.02% NP-40). The reaction was stopped with addition of 2X Laemmli sample buffer containing 10% β-mercapto-ethanol.

Immunoblotting

Protein samples were heated at 95°C for 5 minutes before loading onto SDS-PAGE. The proteins were separated on SDS-PAGE cassette (Thermo Fisher Scientific Bolt™ 4-12% Bis-Tris Plus Gels) in 1x MES running buffer. For direct protein detection, the SDS-PAGE was stained using InstantBlue® Protein Stain (Expedeon). For immunoblotting, the separated proteins were transferred onto polyvinylidene difluoride (PVDF) membrane using iBlot™ 2 Dry Blotting System (ThermoFisher Scientific). The blot was blocked with 5% skim milk in PBS containing 0.05% Tween-20 and probed with anti-mono or poly ADP-ribose binding antibodies MABE1076 (α-MAR), MABC547 (α-PAR), MABE1075 (α-MAR/PAR) (Millipore-Sigma) and anti-GST tag monoclonal antibody MA4-004 (ThermoFisher Scientific). The primary antibodies were detected with secondary infrared anti-rabbit and anti-mouse antibodies (LI-COR Biosciences). All immunoblots were visualized using Odyssey® CLx Imaging System (LI-COR Biosciences).

Structure Determination

Crystallization and Data Collection: Purified SARS-CoV-2 Mac1 in 150mM NaCl, 20mM Tris pH 8.0 was concentrated to 13.8 mg/mL for crystallization screening. All crystallization experiments were setup using an NT8 drop-setting robot (Formulatrix Inc.) and UVXPO MRC (Molecular Dimensions) sitting drop vapor diffusion plates at 18°C. 100 nL of protein and 100 nL crystallization solution were dispensed and equilibrated against 50 uL of the latter. The SARS-CoV-2 Mac1 complex with ADP-ribose was prepared by adding the ligand, from a 100 mM stock in water, to the protein at a final concentration of 2 mM. Crystals that were obtained in 1-2 days from the Salt Rx HT screen (Hampton Research) condition E10 (1.8 M NaH_2PO_4/K_2HPO_4, pH 8.2). Refinement screening was conducted using the additive screen HT

(Hampton Research) by supplementing 10% of each additive to the Salt Rx HT E10 condition in a new 96-well UVXPO crystallization plate. The crystals used for data collection were obtained from Salt Rx HT E10 supplemented with 0.1 M NDSB-256 from the additive screen (Fig. S1). Samples were transferred to a fresh drop composed of 80% crystallization solution and 20% (v/v) PEG 200 and stored in liquid nitrogen. X-ray diffraction data were collected at the Advanced Photon Source, IMCA-CAT beamline 17-ID using a Dectris Eiger 2X 9M pixel array detector.

Structure Solution and Refinement: Intensities were integrated using XDS[35,36] via Autoproc[37] and the Laue class analysis and data scaling were performed with Aimless[38]. Notably, a pseudo-translational symmetry peak was observed at (0, 0.31 0.5) that was 44.6% of the origin. Structure solution was conducted by molecular replacement with Phaser[39] using a previously determined structure of ADP-ribose bound SARS-CoV-2 Mac1 (PDB 6W02) as the search model. The top solution was obtained in the space group $P2_1$ with four molecules in the asymmetric unit. Structure refinement and manual model building were conducted with Phenix[40] and Coot[41] respectively. Disordered side chains were truncated to the point for which electron density could be observed. Structure validation was conducted with Molprobity[42] and figures were prepared using the CCP4MG package[43]. Superposition of the macrodomain structures was conducted with GESAMT[44].

Statistical Analysis

All statistical analyses were done using an unpaired two-tailed student's t-test to assess differences in mean values between groups, and graphs are expressed as mean ±SD. Significant p values are denoted with *$p \leq 0.05$.

ACCESSION CODES

The coordinates and structure factors for SARS-CoV-2 Mac1 were deposited to the Worldwide Protein Databank (wwPDB) with the accession code 6WOJ.

ACKNOWLEDGEMENTS

We'd like to thank Drs. Ivan Ahel and Gytis Jankevicius for providing protein expression plasmids. This research was funded by the National Institutes of Health (NIH), grant numbers P20 GM113117, P30GM110761, and AI134993-01 to A.R.F. Use of the IMCA-CAT beamline 17-ID at the Advanced Photon Source was supported by the companies of the Industrial Macromolecular Crystallography Association through a contract with Hauptman-Woodward Medical Research Institute. Use of the Advanced Photon Source was supported by the U.S. Department of Energy, Office of Science, Office of Basic Energy Sciences, under Contract No. DE-AC02-06CH11357.

REFERENCES

1. Zhou, P. et al. A pneumonia outbreak associated with a new coronavirus of probable bat origin. *Nature* **579**, 270-273 (2020).
2. Coronaviridae Study Group of the International Committee on Taxonomy of Viruses. The species Severe acute respiratory syndrome-related coronavirus: classifying 2019-nCoV and naming it SARS-CoV-2. *Nat Microbiol* **5**, 536-544 (2020).
3. Srinivasan, S. et al. Structural Genomics of SARS-CoV-2 Indicates Evolutionary Conserved Functional Regions of Viral Proteins. *Viruses* **12**, 360 (2020).
4. Wu, C. et al. Analysis of therapeutic targets for SARS-CoV-2 and discovery of potential drugs by computational methods. *Acta Pharm Sin B* (2020).
5. Fehr, A.R. & Perlman, S. Coronaviruses: An Overview of Their Replication and Pathogenesis. in *Coronaviruses*, Vol. 1282 (eds. Maier, H.J., Bickerton, E. & Britton, P.) 1-23 (Springer New York, 2015).
6. Egloff, M.P. et al. Structural and functional basis for ADP-ribose and poly(ADP-ribose) binding by viral macro domains. *J Virol* **80**, 8493-502 (2006).
7. Putics, A., Filipowicz, W., Hall, J., Gorbalenya, A.E. & Ziebuhr, J. ADP-ribose-1"-monophosphatase: a conserved coronavirus enzyme that is dispensable for viral replication in tissue culture. *J Virol* **79**, 12721-31 (2005).
8. Saikatendu, K.S. et al. Structural basis of severe acute respiratory syndrome coronavirus ADP-ribose-1"-phosphate dephosphorylation by a conserved domain of nsP3. *Structure* **13**, 1665-75 (2005).
9. Cho, C.C., Lin, M.H., Chuang, C.Y. & Hsu, C.H. Macro Domain from Middle East Respiratory Syndrome Coronavirus (MERS-CoV) Is an Efficient ADP-ribose Binding Module: CRYSTAL STRUCTURE AND BIOCHEMICAL STUDIES. *J Biol Chem* **291**, 4894-902 (2016).
10. Xu, Y. et al. Crystal structures of two coronavirus ADP-ribose-1"-monophosphatases and their complexes with ADP-Ribose: a systematic structural analysis of the viral ADRP domain. *J Virol* **83**, 1083-92 (2009).
11. Makrynitsa, G.I. et al. Conformational plasticity of the VEEV macro domain is important for binding of ADP-ribose. *J Struct Biol* **206**, 119-127 (2019).
12. Malet, H. et al. The crystal structures of Chikungunya and Venezuelan equine encephalitis virus nsP3 macro domains define a conserved adenosine binding pocket. *J Virol* **83**, 6534-45 (2009).
13. Rack, J.G., Perina, D. & Ahel, I. Macrodomains: Structure, Function, Evolution, and Catalytic Activities. *Annu Rev Biochem* **85**, 431-54 (2016).
14. Li, C. et al. Viral Macro Domains Reverse Protein ADP-Ribosylation. *J Virol* **90**, 8478-86 (2016).
15. Eckei, L. et al. The conserved macrodomains of the non-structural proteins of Chikungunya virus and other pathogenic positive strand RNA viruses function as mono-ADP-ribosylhydrolases. *Sci Rep* **7**, 41746 (2017).
16. Fehr, A.R. et al. The Conserved Coronavirus Macrodomain Promotes Virulence and Suppresses the Innate Immune Response during Severe Acute Respiratory Syndrome Coronavirus Infection. *mBio* **7**, e01721-16 (2016).

17. Kim, D.S., Challa, S., Jones, A. & Kraus, W.L. PARPs and ADP-ribosylation in RNA biology: from RNA expression and processing to protein translation and proteostasis. *Genes Dev* **34**, 302-320 (2020).
18. Fehr, A.R. et al. The impact of PARPs and ADP-ribosylation on inflammation and host-pathogen interactions. *Genes Dev* **34**, 341-359 (2020).
19. Eriksson, K.K., Cervantes-Barragan, L., Ludewig, B. & Thiel, V. Mouse hepatitis virus liver pathology is dependent on ADP-ribose-1"-phosphatase, a viral function conserved in the alpha-like supergroup. *J Virol* **82**, 12325-34 (2008).
20. Fehr, A.R. et al. The nsp3 macrodomain promotes virulence in mice with coronavirus-induced encephalitis. *J Virol* **89**, 1523-36 (2015).
21. Grunewald, M.E. et al. The coronavirus macrodomain is required to prevent PARP-mediated inhibition of virus replication and enhancement of IFN expression. *PLoS Pathog* **15**, e1007756 (2019).
22. Alhammad, Y.M.O. & Fehr, A.R. The Viral Macrodomain Counters Host Antiviral ADP-Ribosylation. *Viruses* **12**, 384 (2020).
23. Abraham, R. et al. ADP-ribosyl-binding and hydrolase activities of the alphavirus nsP3 macrodomain are critical for initiation of virus replication. *Proc Natl Acad Sci U S A* **115**, E10457-E10466 (2018).
24. Abraham, R. et al. Both ADP-Ribosyl-Binding and Hydrolase Activities of the Alphavirus nsP3 Macrodomain Affect Neurovirulence in Mice. *mBio* **11**(2020).
25. McPherson, R.L. et al. ADP-ribosylhydrolase activity of Chikungunya virus macrodomain is critical for virus replication and virulence. *Proc Natl Acad Sci U S A* **114**, 1666-1671 (2017).
26. Parvez, M.K. The hepatitis E virus ORF1 'X-domain' residues form a putative macrodomain protein/Appr-1"-pase catalytic-site, critical for viral RNA replication. *Gene* **566**, 47-53 (2015).
27. Vuksanovic, N., Silvaggi, N.R. National Science Foundation (NSF, United States). High-resolution structure of the SARS-CoV-2 NSP3 Macro X domain doi: 10.2210/pdb6WEY/pdb. (2020).
28. Michalska, K., Stols, L., Jedrzejczak, R., Endres, M., Babnigg, G., Kim, Y., Joachimiak, A., Center for Structural Genomics of Infectious Diseases (CSGID). Crystal Structure of ADP ribose phosphatase of NSP3 from SARS-CoV-2 in the apo doi: 10.2210/pdb6WEN/pdb. (2020).
29. Michalska, K., Kim, Y., Jedrzejczak, R., Maltseva, N., Endres, M., Mececar, A., Joachimiak, A., Center for Structural Genomics of Infectious Diseases (CSGID). Crystal Structure of ADP ribose phosphatase of NSP3 from SARS CoV-2 in the complex with ADP ribose doi: 10.2210/pdb6W02/pdb. (2020).
30. Jankevicius, G. et al. A family of macrodomain proteins reverses cellular mono-ADP-ribosylation. *Nat Struct Mol Biol* **20**, 508-14 (2013).
31. Shull, N.P., Spinelli, S.L. & Phizicky, E.M. A highly specific phosphatase that acts on ADP-ribose 1"-phosphate, a metabolite of tRNA splicing in Saccharomyces cerevisiae. *Nucleic Acids Res* **33**, 650-60 (2005).
32. Rosenthal, F. et al. Macrodomain-containing proteins are new mono-ADP-ribosylhydrolases. *Nat Struct Mol Biol* **20**, 502-7 (2013).
33. Sharifi, R. et al. Deficiency of terminal ADP-ribose protein glycohydrolase TARG1/C6orf130 in neurodegenerative disease. *EMBO J* **32**, 1225-37 (2013).

34. Gibson, B.A., Conrad, L.B., Huang, D. & Kraus, W.L. Generation and Characterization of Recombinant Antibody-like ADP-Ribose Binding Proteins. *Biochemistry* **56**, 6305-6316 (2017).
35. Kabsch, W. Evaluation of single-crystal X-ray diffraction data from a position-sensitive detector. *Journal of Applied Crystallography* **21**, 916-924 (1988).
36. Kabsch, W. Xds. *Acta Crystallogr D Biol Crystallogr* **66**, 125-32 (2010).
37. Vonrhein, C. et al. Data processing and analysis with the autoPROC toolbox. *Acta Crystallogr D Biol Crystallogr* **67**, 293-302 (2011).
38. Evans, P.R. An introduction to data reduction: space-group determination, scaling and intensity statistics. *Acta Crystallogr D Biol Crystallogr* **67**, 282-92 (2011).
39. McCoy, A.J. et al. Phaser crystallographic software. *J Appl Crystallogr* **40**, 658-674 (2007).
40. Adams, P.D. et al. PHENIX: a comprehensive Python-based system for macromolecular structure solution. *Acta Crystallogr D Biol Crystallogr* **66**, 213-21 (2010).
41. Emsley, P., Lohkamp, B., Scott, W.G. & Cowtan, K. Features and development of Coot. *Acta Crystallogr D Biol Crystallogr* **66**, 486-501 (2010).
42. Chen, V.B. et al. MolProbity: all-atom structure validation for macromolecular crystallography. *Acta Crystallogr D Biol Crystallogr* **66**, 12-21 (2010).
43. Potterton, L. et al. Developments in the CCP4 molecular-graphics project. *Acta Crystallogr D Biol Crystallogr* **60**, 2288-94 (2004).
44. Krissinel, E. Enhanced fold recognition using efficient short fragment clustering. *Journal of molecular biochemistry* **1**, 76 (2012).
45. Evans, P. Scaling and assessment of data quality. *Acta Crystallogr D Biol Crystallogr* **62**, 72-82 (2006).
46. Diederichs, K. & Karplus, P.A. Improved R-factors for diffraction data analysis in macromolecular crystallography. *Nat Struct Biol* **4**, 269-75 (1997).
47. Weiss, M.S. Global indicators of X-ray data quality. *Journal of Applied Crystallography* **34**, 130-135 (2001).
48. Evans, P. Resolving Some Old Problems in Protein Crystallography. *Science* **336**, 986-987 (2012).
49. Karplus, P.A. & Diederichs, K. Linking crystallographic model and data quality. *Science* **336**, 1030-3 (2012).

Table 1. Crystallographic data for SARS-CoV-2 Mac1.

	SARS-CoV-2 Mac1
Data Collection	
Unit-cell parameters (Å, °)	a=59.72, b=83.17, c=84.24, β=94.4
Space group	$P2_1$
Resolution (Å)[1]	48.41-2.20 (2.27-2.20)
Wavelength (Å)	1.0000
Temperature (K)	100
Observed reflections	144,767
Unique reflections	41,586
$\langle I/\sigma(I)\rangle$[1]	7.3 (1.9)
Completeness (%)[1]	99.4 (99.7)
Multiplicity[1]	3.5 (3.4)
R_{merge} (%)[1,2]	13.0 (67.0)
R_{meas} (%)[1,4]	15.4 (79.2)
R_{pim} (%)[1,4]	8.2 (41.8)
$CC_{1/2}$ [1,5]	0.994 (0.849)
Refinement	
Resolution (Å)[1]	42.00-2.20
Reflections (working/test)[1]	39,474/1,966
R_{factor} / R_{free} (%)[1,3]	19.9/25.2
No. of atoms (Protein/Ligand/Water)	4,930/144/358
Model Quality	
R.m.s deviations	
Bond lengths (Å)	0.011
Bond angles (°)	1.144
Mean B-factor (Å)[2]	
All Atoms	28.1
Protein	27.9
Ligand	26.0
Water	30.9
Coordinate error (maximum likelihood) (Å)	0.31
Ramachandran Plot	
Most favored (%)	97.3
Additionally allowed (%)	2.4

1) Values in parenthesis are for the highest resolution shell.
2) $R_{merge} = \Sigma_{hkl}\Sigma_I |I_i(hkl) - \langle I(hkl)\rangle| / \Sigma_{hkl}\Sigma_I I_i(hkl)$, where $I_i(hkl)$ is the intensity measured for the ith reflection and $\langle I(hkl)\rangle$ is the average intensity of all reflections with indices hkl.
3) $R_{factor} = \Sigma_{hkl} ||F_{obs}(hkl)| - |F_{calc}(hkl)|| / \Sigma_{hkl} |F_{obs}(hkl)|$; Rfree is calculated in an identical manner using 5% of randomly selected reflections that were not included in the refinement.
4) R_{meas} = redundancy-independent (multiplicity-weighted) R_{merge}[38,45]. R_{pim} = precision-indicating (multiplicity-weighted) R_{merge}[46,47]
5) $CC_{1/2}$ is the correlation coefficient of the mean intensities between two random half-sets of data[48,49]

FIGURE LEGENDS

Figure 1. The SARS-CoV-2 Mac1 is a small domain within nsp3 and is highly conserved between other human CoV Mac1 protein domains. **(A)** Cartoon Schematic of the SARS-CoV-2 non-structural protein 3. The conserved macrodomain, or Mac1, is highlighted in yellow. **(B)** Sequence alignment of Mac1 from the highly-pathogenic human CoVs. Sequences were aligned using the ClustalW method from Clustal Omega online tool with manual adjustment. Identical residues are bolded, shaded in grey, and marked with asterisks.

Figure 2. Structure of SARS-CoV-2 Mac1 complexed with ADP-ribose. **A)** The structure was rendered as a blend through model from the N-terminus (blue) to the C-terminus (red). **B)** The structure was colored by secondary structure showing sheets (magenta) and helices (green). The ADP-ribose is rendered as gray cylinders with oxygens and nitrogens colored red and blue, respectively.

Figure 3. Binding mode of ADP-ribose in SARS-CoV-2 Mac1. **A)** Fo-Fc Polder omit map (green mesh) contoured at 3σ. **B)** Hydrogen bond interactions (dashed lines) between ADP-ribose and amino acids. **C)** Interactions with water molecules. Direct hydrogen bond interactions are represented by dashed lines and water mediated contacts to amino acids are drawn as solid lines.

Figure 4. Superposition of SARS-CoV-2 macrodomain (magenta) with coronavirus macrodomain structures. **A**) SARS-CoV Mac1 with ADP-ribose (gold) (2FAV) and **B**) MERS-CoV Mac1 with ADP-ribose (teal) (5HOL). Superposition of SARS-CoV-2 Mac1 (magenta) with other coronavirus Mac1 structures highlighting the ADP-ribose binding site. **C**) SARS-CoV (gold), **D**) MERS-CoV (teal). The ADP-ribose molecules are colored gray for SARS-CoV-2

572 Mac1 (**A-D**) and are rendered as green cylinders for SARS-CoV Mac1 (panel **A,C**) and MERS-
573 CoV Mac1 (panel **B,D**).

574 **Figure 5**. Human CoVs bind to ADP-ribose with similar affinity. **A-B)** ADP-ribose binding of
575 human Mdo2 and SARS-CoV, MERS-CoV, and SARS-CoV-2 Mac1 proteins by ITC. Images in
576 **(A)** are of one experiment representative of at least 2 independent experiments. Data in **(B)**
577 represent the combined averages of multiple independent experiments for each protein. Mdo2
578 n=2; SARS-CoV n=5; MERS-CoV n=6; SARS-CoV-2 n=2. **C)** ADP-ribose binding of
579 macrodomain proteins by DSF assay. Mdo2 n=4; SARS-CoV n=6; MERS-CoV n=5; SARS-
580 CoV-2 n=3.

581 **Figure 6**. SARS-CoV-2, SARS-CoV, and MERS-CoV Mac1 proteins are potent ADP-
582 ribosylhydrolases. **A,C)** The SARS-CoV-2 macrodomain **(A)** or multiple macrodomain proteins
583 **(C)** were incubated with MARylated PARP10 CD *in vitro* for the indicated times at 37°C. ADP-
584 ribosylated PARP10 CD was detected by immunoblot (IB) with anti-mono ADP-ribose antibody
585 (Millipore-Sigma MAB1076). Total PARP10 CD and macrodomain protein levels were
586 determined by Coomassie Blue (CB) staining. PARP10 CD incubated alone at 37°C was stopped
587 at 0, 30 or 60 minutes. **B,D)** level of de-ADP-ribosylation was measured by quantifying band
588 intensity using Image J software. Intensity values were plotted and fit to a non-linear regression
589 curve **(B)** or as bar graphs representing the means with error bars representing standard deviation
590 **(D)**. Results in **A** and **C** are representative experiments of two and three independent
591 experiments, respectively. Data in **B** and **D** represent the combined results of two and three
592 independent experiments, respectively. Asterisks indicate statistical significance between these
593 samples and the same timepoint from samples treated with Mdo2.
594

SUPPLEMENTAL FIGURE LEGENDS

Figure S1. Purification and crystallization of macrodomain proteins. **A)** Macrodomain proteins were purified as described in Methods. Equimolar amounts of the recombinant proteins were run on a polyacrylamide gel and visualized by Coomassie staining. **B)** Crystals of SARS-CoV-2 Mac1 obtained with Salt Rx HT E10 supplemented with 0.1 M NDSB-256.

Figure S2. Extended residues at the C-terminus of the SARS-CoV-2 Mac1 clashed with symmetry related molecules. **A)** Comparison of the amino acid sequence of SARS-CoV-2 Mac1, 6W02 and 6WEY. **B)** Superposition of SARS-CoV-2 Mac1 (magenta) subunit B onto subunit A of 6W02 reveals that the C-terminus would clash with symmetry related molecules (coral).

Figure S3. Superposition of SARS-CoV-2 Mac1 (magenta) with other recently determined homologous structures. **A)** SARS-CoV-2 Mac1 apo structure (6WEN), **B)** SARS-CoV-2 Mac1 complexed with ADP-ribose (6W02). The ADP-ribose molecule is colored gray for SARS-CoV-2 and is represented as green cylinders for 6W02 in panel **B**. Comparison of the residues in the ADP-ribose binding site. **C**) SARS-CoV-2 Mac1 apo structure (blue, 6WEN), **D**) SARS-CoV-2 Mac1 complexed with ADP-ribose (green, 6W02). The ADP-ribose of SARS-CoV-2 is rendered as gray cylinders, and is represented as green cylinders for 6W02 in panel **B**.

Figure S4. Affinity of ADP-ribose binding antibodies for ADP-ribosylated PARP10 CD. MARylated PARP10 and non-MARylated PARP10 CD were detected by immunoblot (IB) with anti-GST (Invitrogen, MA4-004), anti-ADP-ribose antibodies: anti-MAR (Millipore-Sigma MAB1076), anti-PAR (Millipore-Sigma MABC547), and anti-MAR/PAR (Millipore-Sigma MABE1075) antibodies.

A

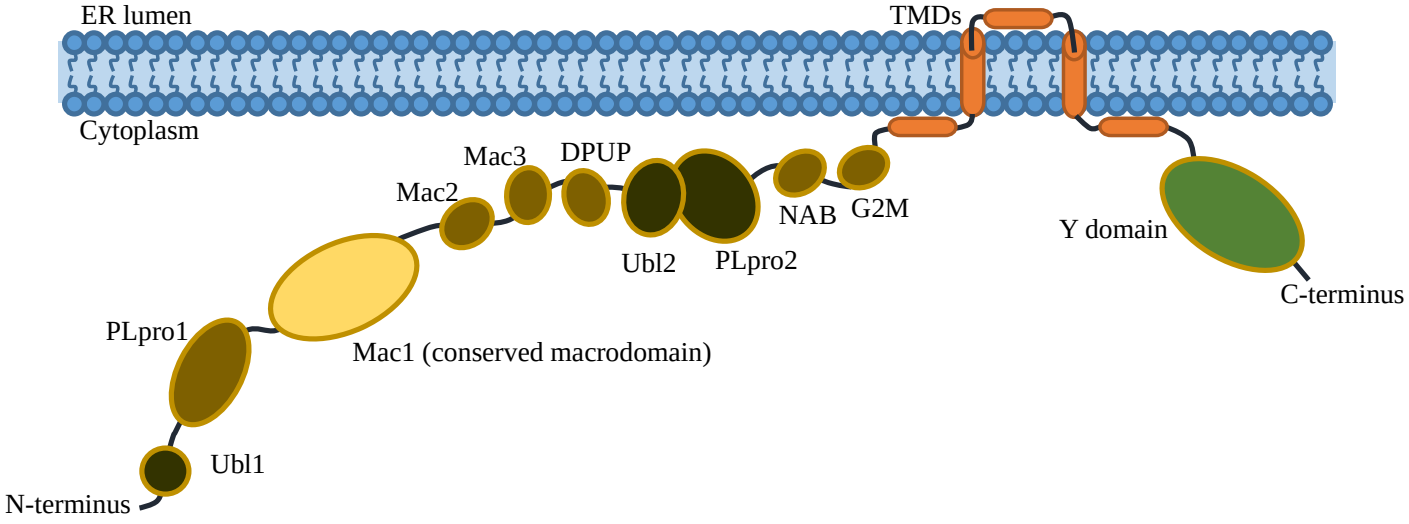

B

```
SARS-CoV-2 aa  1         10        20        30        40        50        58
SARS-CoV-2    --IEVNSFSGYLKLTDNVYIKNADIVEEAKKVKPTVVVNAANVYLKHGGGVAGALNKATN 58
SARS-CoV      --EPVNQFTGYLKLTDNVAIKCVDIVKEAQSANPMVIVNAANIHLKHGGGVAGALNKATN 58
MERS-CoV      NVDPLSNFEHK-VITECVTIVLGDAIQVAKCYGESVLVNAANTHLKHGGGIAGAINAASK 59
                     *      *  * *   *    *       * *****  ****** *** * *

SARS-CoV-2 aa 60        70        80        90        100       110       118
SARS-CoV-2    NAMQVESDDYIATNGPLKVGGSCVLSGHNLAKHCLHVVGPNVNKGEDIQLLKSAYEVFNQ 118
SARS-CoV      GAMQKESDDYIKLNGPLTVGGSCLLSGHNLAKKCLHVVGPNLNAGEDIQLLKAAYENFNS 118
MERS-CoV      GAVQKESDEYILAKGPLQVGDSVLLQGHSLAKNILHVVGPDARAKQDVSLLSKCYKAMNA 119
               * * *** **   *** ** *  * ** ***  ******      *  **   *   *

SARS-CoV-2 aa 120       130       140       150       160       170
SARS-CoV-2    HEVLLAPLLSAGIFGADPIHSLRVCVDTVRTNVYLAVFDKNLYDKLVSSFLEMKSEK  175
SARS-CoV      QDILLAPLLSAGIFGAKPLQSLQVCVQTVRTQVYIAVNDKALYEQVVMDYLDNL-    172
MERS-CoV      YPLVVTPLVSAGIFGVKPAVSFDYLIREAKTRVLVVVNSQDVYKSLTIVDIPQLE    174
                    ** ******  *  *         * *   *     *
```

Figure 1. The SARS-CoV-2 Mac1 is a small domain within nsp3 and is highly conserved between other human CoV Mac1 protein domains. **(A)** Cartoon Schematic of the SARS-CoV-2 non-structural protein 3. The conserved macrodomain, or Mac1, is highlighted in yellow. **(B)** Sequence alignment of Mac1 from the highly-pathogenic human CoVs. Sequences were aligned using the ClustalW method from Clustal Omega online tool with manual adjustment. Identical residues are bolded, shaded in grey, and marked with asterisks.

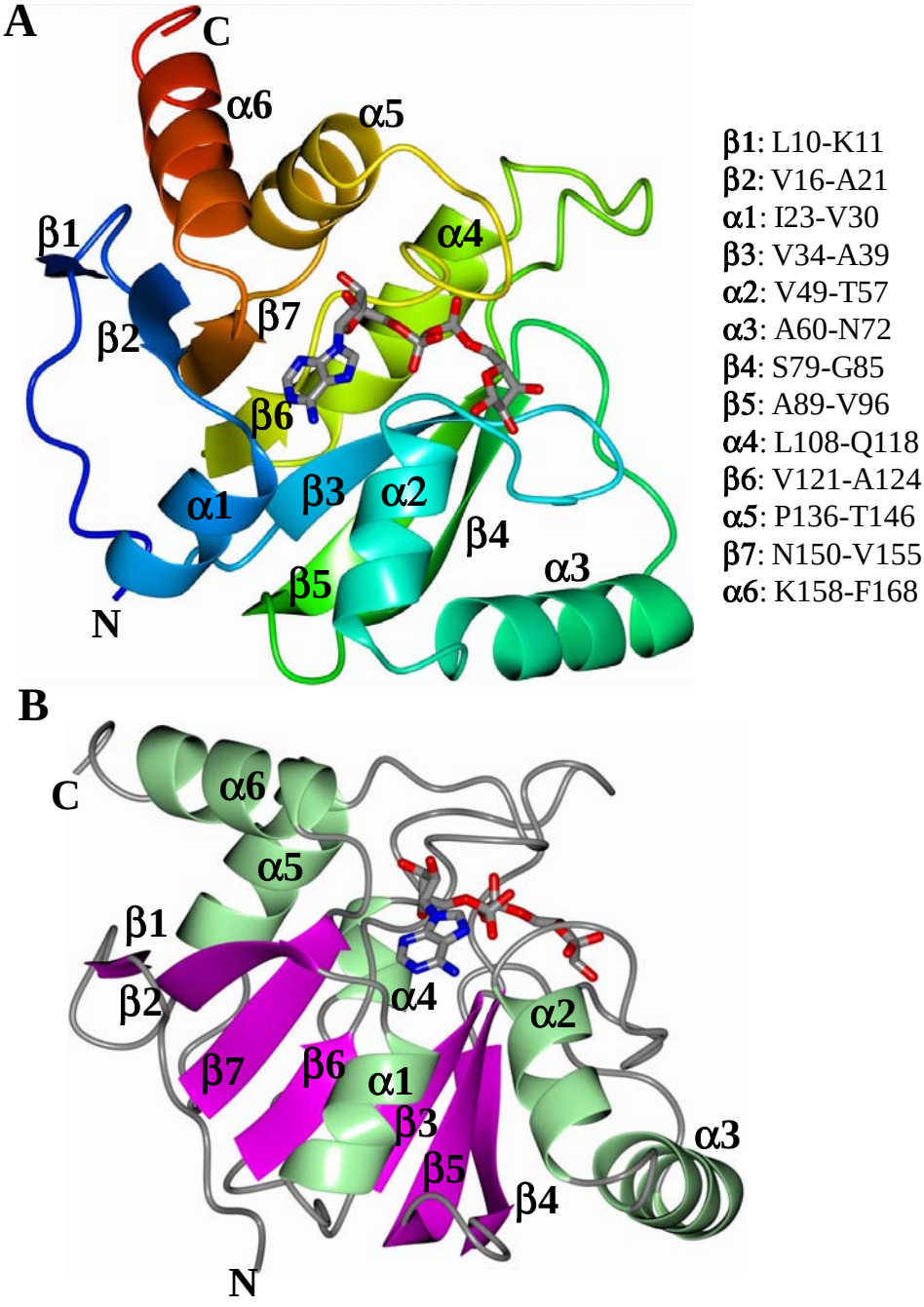

Figure 2. Structure of SARS-CoV-2 Mac1 complexed with ADP-ribose. **A)** The structure was rendered as a blend through model from the N-terminus (blue) to the C-terminus (red). **B)** The structure was colored by secondary structure showing sheets (magenta) and helices (green). The ADP-ribose is rendered as gray cylinders with oxygens and nitrogens colored red and blue, respectively.

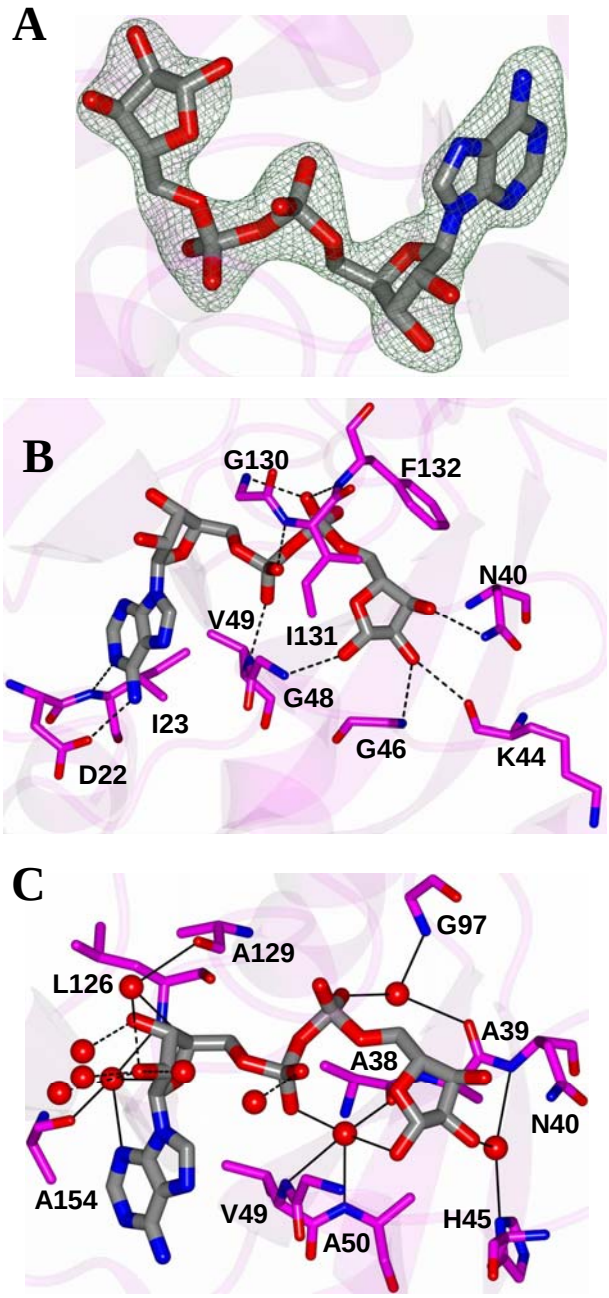

Figure 3. Binding mode of ADP-ribose in SARS-CoV-2 Mac1. **A)** Fo-Fc Polder omit map (green mesh) contoured at 3σ. **B)** Hydrogen bond interactions (dashed lines) between ADP-ribose and amino acids. **C)** Interactions with water molecules. Direct hydrogen bond interactions are represented by dashed lines and water mediated contacts to amino acids are drawn as solid lines.

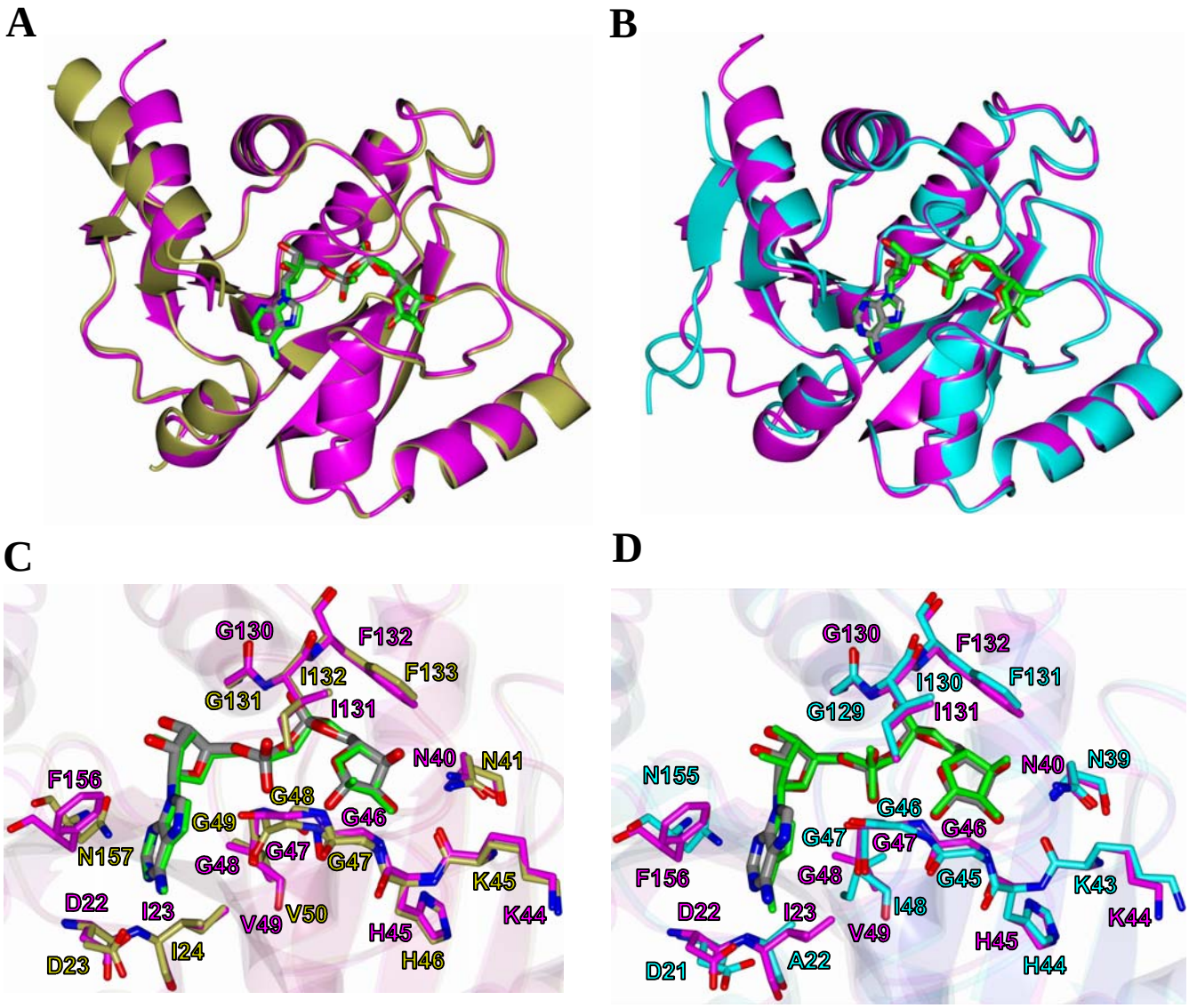

Figure 4. Superposition of SARS-CoV-2 macrodomain (magenta) with coronavirus macrodomain structures. **A**) SARS-CoV Mac1 with ADP-ribose (gold) (2FAV) and **B**) MERS-CoV Mac1 with ADP-ribose (teal) (5HOL). Superposition of SARS-CoV-2 Mac1 (magenta) with other coronavirus Mac1 structures highlighting the ADP-ribose binding site. **C**) SARS-CoV (gold), **D**) MERS-CoV (teal). The ADP-ribose molecules are colored gray for SARS-CoV-2 (A-D) and are rendered as green cylinders for SARS-CoV Mac1 (panel A,C) and MERS-CoV Mac1 (panel B,D).

A

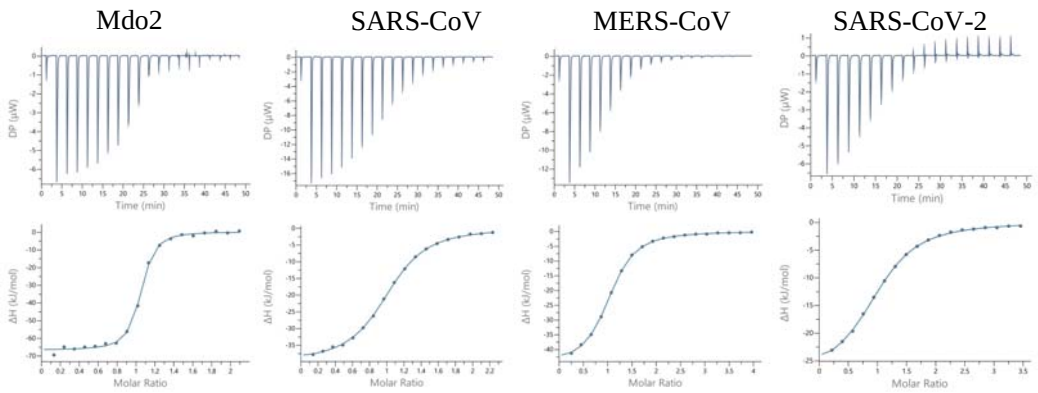

B

Macrodomain	Stoichiometry (N)	Kd (uM)	ΔH (kcal/mol)	ΔG (kcal/mol)
Mdo2	0.92 ± 0.01	0.24 ± 0.02	-66 ± 1	-38 ± 2
SARS-CoV	0.89 ± 0.04	10.8 ± 1.7	-40 ± 1.2	-28 ± 0.4
MERS-CoV	0.97 ± 0.04	7.9 ± 0.15	-47 ± 3	-29 ± 0.4
SARS-CoV-2	1.14 ± 0.06	16.8 ± 0.04	-28 ± 0.1	-27 ± 0.1

C

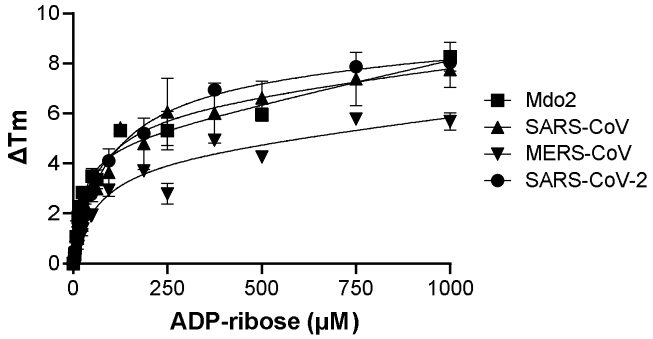

Figure 5. Human CoVs bind to ADP-ribose with similar affinity. **A-B)** ADP-ribose binding of human Mdo2 and SARS-CoV, MERS-CoV, and SARS-CoV-2 Mac1 proteins by ITC. Images in **(A)** are of one experiment representative of at least 2 independent experiments. Data in **(B)** represent the combined averages of multiple independent experiments for each protein. Mdo2 n=2; SARS-CoV n=5; MERS-CoV n=6; SARS-CoV-2 n=2. **C)** ADP-ribose binding of macrodomain proteins by DSF assay. Mdo2 n=4; SARS-CoV n=6; MERS-CoV n=5; SARS-CoV-2 n=3.

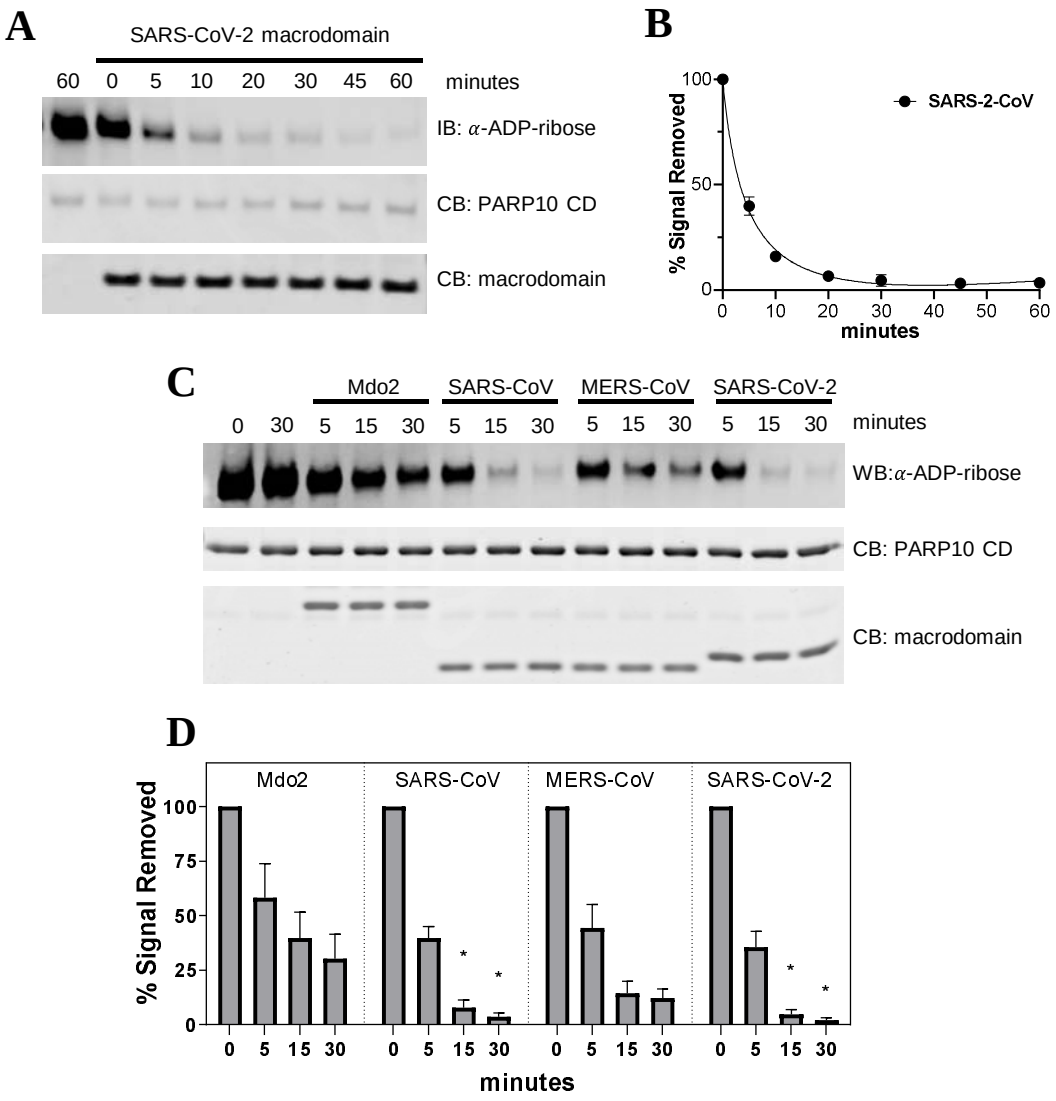

Figure 6. SARS-CoV-2, SARS-CoV, and MERS-CoV Mac1 proteins are potent ADP-ribosylhydrolases. **A,C)** The SARS-CoV-2 macrodomain **(A)** or multiple macrodomain proteins **(C)** were incubated with MARylated PARP10 CD *in vitro* for the indicated times at 37°C. ADP-ribosylated PARP10 CD was detected by immunoblot (IB) with anti-ADP-ribose antibody (Millipore-Sigma MAB1076). Total PARP10 CD and macrodomain protein levels were determined by Coomassie Blue (CB) staining. PARP10 CD incubated alone at 37°C was stopped at 0, 30 or 60 minutes. **B,D)** level of de-ADP-ribosylation was measured by quantifying band intensity using Image J software. Intensity values were plotted and fit to a non-linear regression curve **(B)** or as bar graphs representing the means with error bars representing standard deviation **(D)**. Results in **A** and **C** are representative experiments of two and three independent experiments, respectively. Data in **B** and **D** represent the combined results of two and three independent experiments, respectively. Asterisks indicate statistical significance between these samples and the same timepoint from samples treated with Mdo2.